Morphological and Functional Modeling of the Heart Valves and Chambers

Razvan Ioan Ionasec, Dime Vitanovski and Dorin Comaniciu

Image Analytics and Informatics, Siemens Corporate Research, Princeton NJ, USA

Abstract Personalized cardiac models have become a crucial component of the clinical workflow, especially in the context of complex cardiovascular disorders, such as valvular heart disease. In this chapter we present a comprehensive framework for the patient-specific modeling of the valvular apparatus and heart chambers from multimodal cardiac images. An integrated model of the four heart valves and chambers is introduced, which captures a large spectrum of morphologic, dynamic and pathologic variations. The patient-specific model parameters are estimated from four-dimensional cardiac images using robust learning-based techniques. These include object localization, rigid and non-rigid motion estimation, and surface boundary estimation from dense 4D data (TEE, CT) as well as regression-based techniques for surface reconstruction from sparse 4D data (MRI). Clinical applications based on the patient-specific modeling approach are proposed for decision support in Transcatheter Aortic Valve Implantation and Percutaneous Pulmonary Valve Implantation while performance evaluation is conducted on a population of 476 patients.

1 Introduction

The unprecedented increase in life expectancy over the current and past century propelled Cardiovascular Disease (CVD) to become the deadliest plague, which today causes approximately 30% of fatalities worldwide and nearly 40% in high-income regions. Valvular Heart Disease (VHD) is a representative class of CVD, which affects 2.5% of the global population and requires yearly over 100,000 surgeries in the United States alone. Yet, heart valve operations are the most expensive and riskiest cardiac procedures, with an average cost of $141,120 and 4.9% in-hospital death rate (Lloyd-Jones et al. (2009)).

Due to the strong anatomical, functional and hemodynamic inter-dependency of the heart valves, VHDs do not affect only a single valve, but rather several valves are impaired. Recent studies demonstrate strong influence of pulmonary artery systolic pressure on the tricuspid regurgitation severity (Mutlak et al. (2009)). In Lansac

Razvan Ioan Ionasec
Image Analytics and Informatics, Siemens Corporate Research, Princeton NJ, USA,
e-mail: razvan.ionasec@siemens.com

et al. (2002); Timek et al. (2003) the simultaneous evaluation of aortic and mitral valves is encouraged, given the fibrous aortic-mitral continuity, which anchors the left side valves and facilitates the reciprocal opening and closing motion during the cardiac cycle. Moreover, in patients with mitral and tricuspid valve regurgitation, joint surgery is recommended to minimize the risk for successive heart failure or reduced functional capacity. Morphological and functional assessment of the complete heart valve apparatus is crucial for clinical decision making during diagnosis and severity assessment as well as treatment selection and planning.

Decisions in valvular disease management increasingly rely on non-invasive imaging. Techniques like Transesophageal Echocardiography (TEE), cardiac Computed Tomography (CT) and Cardiovascular Magnetic Resonance (CMR) imaging, enable dynamic four dimensional scanning of the beating heart over the whole cardiac cycle. Precise morphological and functional knowledge about the valvular apparatus is highly esteemed and it is considered a prerequisite for the entire clinical workflow including diagnosis, therapy-planning, surgery or percutaneous intervention as well as patient monitoring and follow-up. Nevertheless, most non-invasive investigations to date are based on two-dimensional images, user-dependent processing and manually performed, potentially inaccurate measurements (Bonow et al. (2006)).

The progress in medical imaging is matched by important advances in surgical techniques, bioprosthetic valves, robotic surgery and percutaneous interventions, which have led to a twofold increase in the number of valve procedures performed in the United States since 1985 (Jablokow (2009)). There has been a major trend in cardiac therapy towards minimally invasive transcatheter procedures to reduce the side effects of classical surgical techniques. Without direct access and view to the affected structures those interventions are usually performed in so-called Hybrid ORs, equipped with advanced imaging technology. Thus, procedures such as the Transcatheter Aortic Valve Implantation (TAVI) are permanently guided via real-time intra-operative images provided by X-ray Fluoroscopy and Transesophageal Echocardiography systems (Agarwal and Triggs (2004)). Powerful computer-aided tools for extensive non-invasive assessment, planning and guidance are mandatory to continuously decrease the level of invasiveness and maximize effectiveness of valve therapy.

Except for the past decade, cardiac modeling was almost exclusively focused on the left ventricle (LV) (Park et al. (1996); Staib and Duncan (1996)). Rueckert and Burger (1997); Fritz et al. (2006) achieved a combined model of the two ventricles, LV and right ventricle (RV). Few methods in the literature also consider the left and right atria (Zheng et al. (2008); Lorenz and von Berg (2006); Zhuang et al. (2010a); Huang et al. (2007); Zhuang et al. (2010b); Ecabert et al. (2008)), but none explicitly handle the heart valves. The majority of existent valve models presented in the literature are generic and rough approximations of the true valvular anatomy. Their primary application is the analysis of the blood-tissue interaction during the cardiac cycle as well as mechanical and functional behavior of the valvular apparatus. The first cardiac model to include the heart valves was proposed by Peskin and McQueen (1996). De Hart et al. (2002) introduced a refined computational model of the aortic

valve while Soncini et al. (2009) presented a realistic finite element model of the physiological aortic root from medical imaging data. Kunzelman et al. (2007) introduced the first three-dimensional finite element model of the mitral valve. Votta et al. (2008) presented an extended mitral valve model based on *in vivo* data. Watanabe et al. (2005) introduced a geometrical model of the mitral valve, obtained from real-time three-dimensional TEE. The study by Veronesi et al. (2009b) also considers the aortic valve to investigate the functional dependency between the two left-side valves. Schievano et al. (2007b) proposed an analysis protocol of the pulmonary trunk based on rapid prototyping systems. Recently introduced models of the aortic valve (Waechter and et al. (2010), Ionasec et al. (2008b)), the mitral valve (Schneider et al. (2010), Conti et al. (2010)) aortic-mitral coupling (Ionasec et al. (2009a); Veronesi et al. (2009a), Ionasec et al. (2010)) address important aspect of data-driven valve models, yet do not offer a unified approach for the patient-specific modeling of the entire valvular apparatus.

In this chapter we present a complete patient-specific model of the valvular apparatus and heart chambers estimated from multi-modal cardiac images. Section 2 describes a morphological and functional representation of the aortic, mitral, tricuspid and pulmonary valves as well as the four heart chambers. The patient-specific parameters of the cardiac models are estimated from four-dimensional cardiac images using learning-based methods. Section 3 describes robust algorithms for object localization and rigid motion estimation, non-rigid motion estimation, and surface boundary estimation from dense 4D data (Computed Tomography and Echocardiography) as well as regression-based techniques for surface reconstruction from sparse 4D data (Magnetic Resonance Imaging). Based on the patient-specific modeling techniques, in section 5 we introduce two clinical applications that support analysis and planning in Transcatheter Aortic Valve Implantation (TAVI) and Percutaneous Pulmonary Valve Implantation (PPVI). Part of this work has been reported in our previous publications (Ionasec et al. (2009b,a); Vitanovski et al. (2009, 2010); Ionasec et al. (2010); Grbić et al. (2010)).

2 Modeling of the Heart Valves and Chambers

This section introduces an explicit mathematical representation of the cardiac valves and chambers that parameterizes relevant clinical aspects observable through non-invasive imaging modalities (see figure 1). The proposed model of the aortic, mitral, tricuspid and pulmonary valves and the four chambers precisely captures morphological, dynamical and pathological variations. To handle the inherent complexity, the representation is structured on three abstraction layers: global location and rigid motion, non-rigid landmark motion model, and comprehensive surface model. Each model abstraction naturally links to anatomical and dynamical aspects at a specific level of detail, while the hierarchical interconnection of the individual parameterizations is driven by the physiology of the valves.

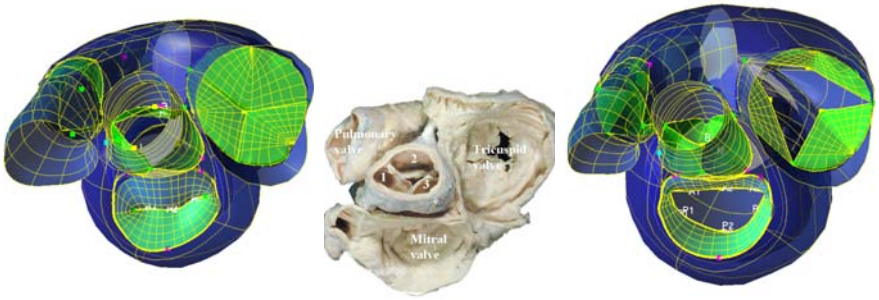

(a) (b) (c)

Fig. 1 The proposed model of the heart valves and chambers in systole (a) and diastole (c). (b) Explanted specimen of the heart valves - Reproduced with permission of the author and the European Association for Cardio-Thoracic Surgery from: Anderson RH. The surgical anatomy of the aortic root. Multimedia Man Cardiothorac Surg doi:10.1510/mmcts.2006.002527.

2.1 Parametrization

Global Location and Rigid Motion: The global location of the valves is parameterized through a similarity transformation in the Euclidean three-dimensional space, which includes nine parameters. A time variable t is augmenting the representation to capture the temporal variation during the cardiac cycle and model the rigid valve motion:

$$\theta(t) = \big\{(c_x, c_y, c_z), (\alpha_x, \alpha_y, \alpha_z), (s_x, s_y, s_z), t\big\} \tag{1}$$

where (c_x, c_y, c_z), $(\alpha_x, \alpha_y, \alpha_z)$, (s_x, s_y, s_z) are the position, orientation and scale parameters. The location and rigid motion of each valve is modeled independently through its individual set of parameters $\theta(t)$, which results into a total of $36 \times T$ parameters for a given volume sequence $I(t)$ of length T.

Non-Rigid Landmark Motion Model: The second abstraction level models anatomical landmarks that are robustly identifiable by doctors, possess a particular visual pattern, and serve as anchor points for qualitative and quantitative clinical assessment. Normalized by the time-dependent similarity transformation, the motion of each anatomical landmark j can be parameterized by its corresponding trajectory $\mathbf{L^j}$ over a full cardiac cycle. For a given volume sequence $I(t)$, one trajectory $\mathbf{L^j}$ is composed by the concatenation of the spatial coordinates:

$$\mathbf{L^j}(\theta_t) = [\mathbf{L^j}(0), \mathbf{L^j}(1), \cdots, \mathbf{L^j}(t), \cdots, \mathbf{L^j}(T-1)] \tag{2}$$

where $\mathbf{L^j}$ are spatial coordinates with $\mathbf{L^j}(t) \in \mathscr{R}^3$ and t an equidistant discrete time variable $t = 0, \cdots, T-1$.

Comprehensive Surface Model: The full geometry of the valves and chambers is modeled using surface meshes constructed along rectangular grids of vertices. For each anatomic structure A_k, the underlying grid is spanned along two physiologically aligned parametric directions, $\mathbf{u}$ and $\mathbf{v}$. Each vertex $\mathbf{p}^{A_k} \in \mathscr{R}^3$ has four neighbors, except the edge and corner points with three and two neighbors, respectively. Therefore, a rectangular grid with $n \times m$ vertices is represented by $(n-1) \times (m-1) \times 2$ triangular faces. The model M of a certain component at a particular time step t is uniquely defined by vertex collections of the anatomic structures A_k. The time parameter t extends the representation to capture dynamics:

$$M(\mathbf{L}^{\mathbf{j}}, \theta_i) = [\overbrace{\left\{\mathbf{p}_0^{A_1}, \cdots, \mathbf{p}_{N_1}^{A_1}\right\}}^{\text{first anatomy}}, \cdots, \overbrace{\left\{\mathbf{p}_0^{A_n}, \cdots, \mathbf{p}_{N_n}^{A_n}\right\}}^{\text{n-th anatomy}}, t] \tag{3}$$

where n is the number of represented anatomies, and $N_1 \ldots N_n$ are the numbers of vertices for a particular anatomy given in the following sections.

2.2 Left-Heart Valves

Aortic Valve: The aortic valve (AV) connects the left ventricular outflow tract to the ascending aorta and includes the aortic root and three leaflets/cusps (left (L) aortic leaflet, right (R) aortic leaflet and none (N) aortic leaflet). The root extends from the basal ring to the sinotubular junction and builds the supporting structure for the leaflets. These are fixed to the root on a crown-like attachment and can be thought of as semi-lunar pockets (see figure 2).

Three aortic commissure points, LR-Comm, NL-Comm and RN-Comm, describe the interconnection locations of the aortic leaflets, while three hinges, L-Hinge, R-Hinge, and N-Hinge, are their lowest attachment points to the root. For each leaflet of the valve, the center of the corresponding free-edge is marked by the leaflet tip point: L/R/N-Tip. The interface between the aorta and coronary arteries is symbolized using the L/R-Ostium, the two coronary ostia (see figure 3(b)).

The anatomical landmarks are also used to describe the global location and rigid motion as follows (see figure 3(a)): $(c_x, c_y, c_z)_{aortic}$ equals to the gravity center of the aortic landmarks, except aortic leaflet tips. α_z is the normal vector to the LR-Comm, NL-Comm, RN-Comm plane, α_x is the unit vector orthogonal to α_z which points from $(c_x, c_y, c_z)_{aortic}$ to LR-Comm, α_y is the cross-product of α_x and α_z. $(s_x, s_y, s_z)_{aortic}$ is given by the maximal distance between the center $(c_x, c_y, c_z)_{aortic}$ and the aortic landmarks, along each of the axes $(\alpha_x, \alpha_y, \alpha_z)$.

Four surface structures represent the aortic valve: aortic root, left coronary leaflet, right coronary leaflet and non coronary leaflet. The aortic root connects the ascending aorta to the left ventricle outflow tract and is represented through a tubular grid (see figure 2(a)). This is aligned with the aortic circumferential $\mathbf{u}$ and ascending directions $\mathbf{v}$ and includes 36×20 vertices and 1368 faces. The root is constrained by six anatomical landmarks, i.e. three commissures and three hinges, with a fixed

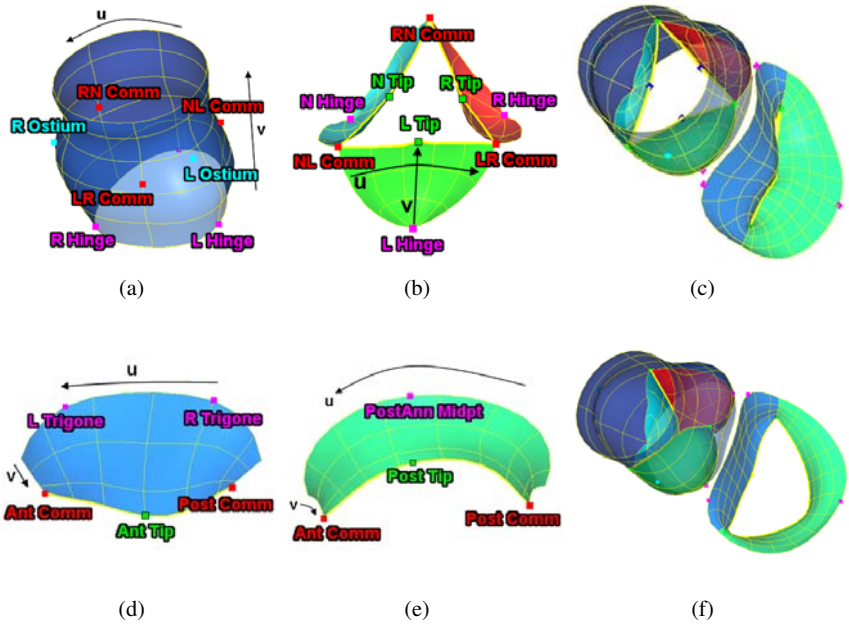

Fig. 2 Isolated surface components of the aortic and mitral models with parametric directions and spatial relations to anatomical landmarks: (a) aortic root, (b) aortic leaflets, (c) aortic-mitral in end-systole, (d) anterior mitral leaflet, (e) posterior mitral leaflet and (f) aortic-mitral in end-diastole.

correspondence on the grid. The three aortic leaflets, the L-, R- and N-leaflet, are modeled as paraboloids on a grid of 11×7 vertices and 120 faces (see figure 2(b)). They are stitched to the root on a crown like attachment ring, which defines the parametric **u** direction at the borders. The vertex correspondence between the root and leaflets along the merging curve is symmetric and kept fixed. The leaflets are constrained by the corresponding hinges, commissures and tip landmarks, where the v direction is the ascending vector from the hinge to the tip (see figure 2(c)).

Mitral Valve: Located in between the left atrium (LA) and the left ventricle (LV), the mitral valve (MV) includes the posterior leaflet, anterior leaflet, annulus and the subvalvular apparatus. The latter consists of the chordae tendiane and papillary muscles, which are not explicitly treated in this work (see figure 2).

The two interconnection points of the mitral leaflets at their free edges are defined by the mitral anterior and posterior commissures, while the mitral annulus is fixed by the L/R-Trigone and posteroannular midpoint (PostAnn MidPoint). The center of the two mitral leaflets' free-edges is marked by the leaflet tip points, the Ant and Post-Tip (anterior/posterior) leaflet tips (see figure 4(b))

The barycentric position $(c_x, c_y, c_z)_{mitral}$ is computed from the mitral landmarks, except mitral leaflet tips (see figure 4(a)). α_z is the normal vector to the L/R-Trigone,

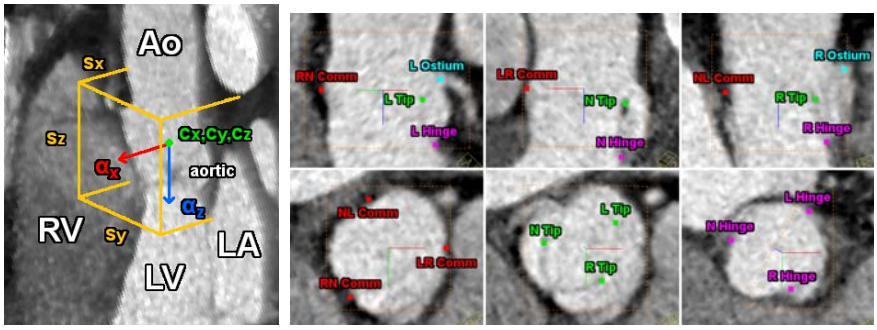

(a) (b)

Fig. 3 Anatomical landmark model of the aortic valve. (a) Perspective view including the bounding box. (b) Landmarks relative to the anatomical location illustrated in long and short axis from an example CT study.

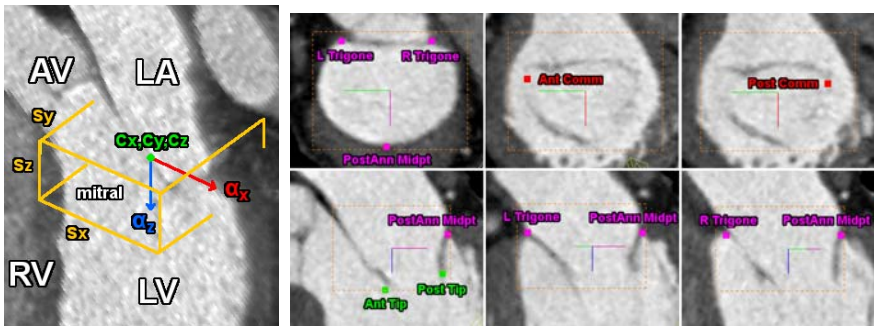

(a) (b)

Fig. 4 Anatomical landmark model of the mitral valve. (a) Perspective view including the bounding box. (b) Landmarks relative to the anatomical location illustrated in long and short axis from an example CT study.

PostAnn MidPoint plane, α_x is orthogonal to α_z and points from $(c_x, c_y, c_z)_{mitral}$ towards the PostAnn MidPoint. The scale parameters $(s_x, s_y, s_z)_{mitral}$ are defined as for the aortic valve, to comprise the entire mitral anatomy.

The mitral leaflets separate the (LA) and (LV) hemodynamically and are connected to the endocardial wall by the saddle shaped mitral annulus. Both are modeled as paraboloids and their upper margins implicitly define the annulus. Their grids are aligned with the circumferential annulus direction **u** and the orthogonal direction **v** pointing from the annulus towards leaflet tips and commissures (see figures 2(d) and 2(e)). The anterior leaflet is constructed from 18×9 vertices and 272 faces while the posterior leaflet is represented with 24×9 vertices and 368 faces. Both leaflets are fixed by the mitral commissures and their corresponding leaflet

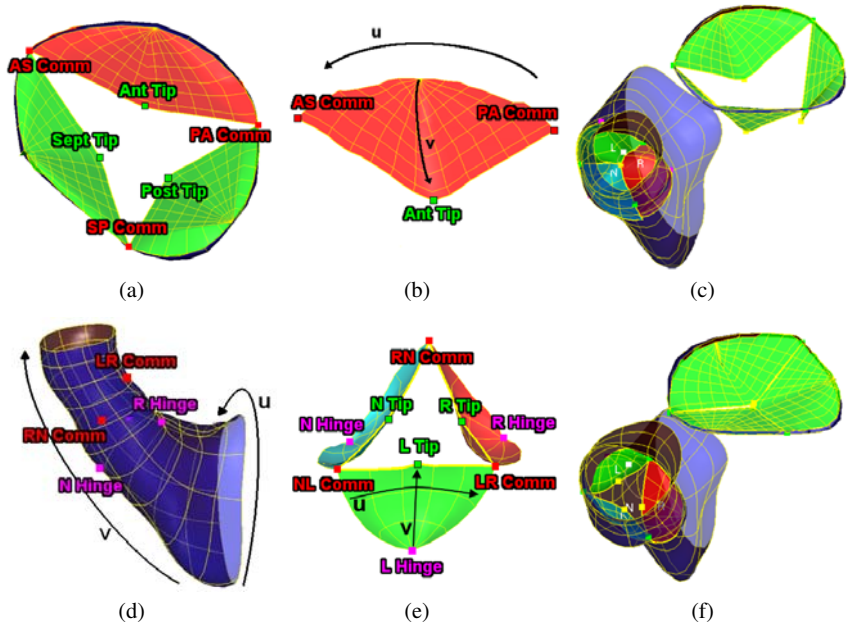

Fig. 5 Isolated surface components of the tricuspid and pulmonary models with parametric directions and spatial relations to anatomical landmarks: (a) tricuspid leaflet, (b) tricuspid annulus and leaflets, (c) tricuspid-pulmonary in end-diastole, (d) pulmonary trunk, (e) pulmonary leaflets and (f) tricuspid-pulmonary in end-systole.

tips. The left / right trigones and the postero-annular midpoint further confine the anterior and posterior leaflets, respectively (see figure 2(f)).

2.3 Right-Heart Valves

Pulmonary Valve: The pulmonary trunk emerges out of the (RV) and branches into the left and right pulmonary arteries, which connect to the corresponding lung. It supports a semilunar valve, geometrically and topologically similar to the aortic valve. The three leaflets of the pulmonary valve (PV) are named according to their relationship with respect to the (AV) as left and right facing leaflet, and none facing leaflet (see figure 5).

Identical as for the aortic valve, three commissure points, LR-Comm, NL-Comm and RN-Comm, describe the interconnection locations of the pulmonary leaflets, while three hinges, L-Hinge, R-Hinge, and N-Hinge, are their lowest attachment points to the pulmonary trunk. For each leaflet of the valve, the center of the corresponding free-edge is marked by the leaflet tip point: L/R/N-Tip. The pulmonary

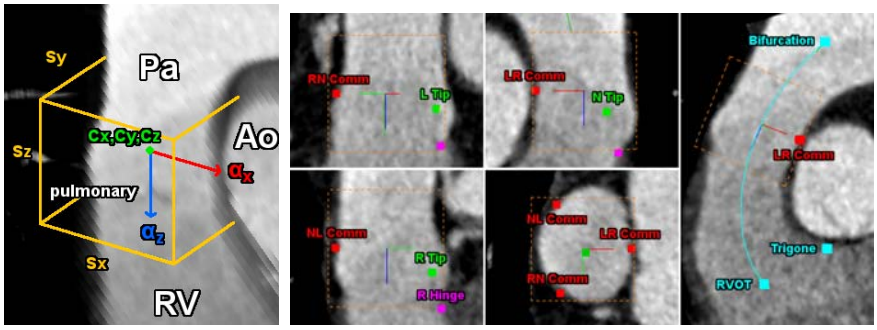

(a) (b)

Fig. 6 Anatomical landmark model of the pulmonary valve. (a) Perspective view including the bounding box. (b) Landmarks relative to the anatomical location illustrated in long and short axis from an example CT study.

trunk is bounded by two landmarks, the RVOT on the right ventricle side and Bifurcation distal to the valve location. The model is completed by right ventricle Trigone landmark (see figure 6(b)).

The location $(c_x, c_y, c_z)_{pulmonary}$ is equal to the gravity center of the commissures and hinges landmarks (see figure 6(b)). α_z is the normal vector to the LR-Comm, NL-Comm, RN-Comm plane, α_x is the unit vector orthogonal to α_z which points from $(c_x, c_y, c_z)_{aortic}$ to LR-Comm, α_y is the cross-product of α_x and α_z. $(s_x, s_y, s_z)_{aortic}$ is given by the maximal distance between the center $(c_x, c_y, c_z)_{aortic}$ and the aortic landmarks, along each of the axes $(\alpha_x, \alpha_y, \alpha_z)$.

The representation of the pulmonary valve is composed out of four structures: pulmonary trunk, left facing leaflet, none facing leaflet and right facing leaflet. The pulmonary trunk emerges out of the right ventricular outflow tract, supports the pulmonary valves and its three leaflets, and ends at the level of the pulmonary artery bifurcation. The grid, which spans the pulmonary trunk surface, is aligned with the circumferential **u** and longitudinal direction v of the valve (see figure 5(d)). It includes 50×40 vertices and 3822 faces confined through the pulmonary commissures, hinges and the (RV) trigone. Additionally, the RVOT and Bifurcation landmarks determine its longitudinal span. The attached L-, R- and N- leaflets, are modeled as paraboloids along the annulus circumferential direction **u** and vector **v** pointing from the corresponding hinge to the leaflet tip (see figure 5(e)). Each includes 11×7 vertices and 120 faces bounded by the associated two commissures, hinge and tip (see figure 5(f)).

Tricuspid Valve: The tricuspid valve (TV), also called the right atrioventricular valve, separates the (RA) from the (RV). It mainly consists of the annulus and subvalvular apparatus as well as three leaflets: septal, inferior and anterosuperior leaflet (see figure 5).

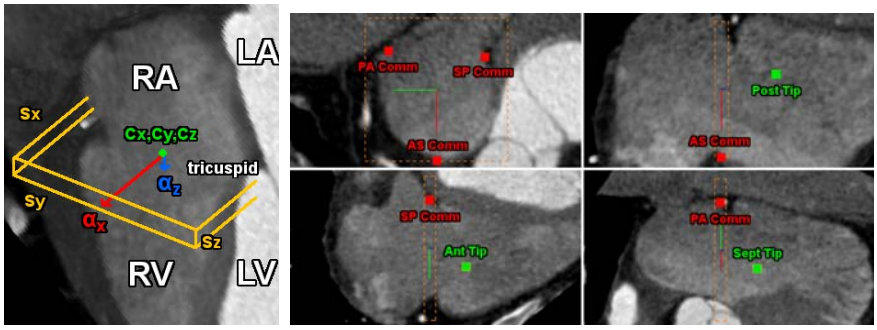

(a) (b)

Fig. 7 Anatomical landmark model of the tricuspid valve. (a) Perspective view including the bounding box. (b) Landmarks relative to the anatomical location illustrated in long and short axis from an example CT study.

The three leaflets of the tricuspid valve, septal-, anterior- and posterior leaflet interconnect in three points marked by three tricuspid commissures, namely the AS Comm, the PA Comm and the SP Comm landmarks. The tricuspid landmark model is completed by the Sept Tip, Ant Tip and Post Tip landmarks, which mark the center of the leaflets' free edge (see figure 7(b)).

The barycentric position $(c_x, c_y, c_z)_{tricuspid}$ is computed from the tricuspid commissures, AS Comm, PA Comm and SP Comm (see figure 7(a)). α_z is the normal vector to the commissural plane, α_x is orthogonal to α_z and points towards the AS Comm. The scale parameters $(s_x, s_y, s_z)_{tricuspid}$ are defined to comprise the entire tricuspid valve anatomy.

The function of the tricuspid valve is to regulate the blood flow from the (RA) to the (RV), staying closed during systole and open during diastole. The model is constrained by three surfaces: septal-, anterior- and posterior leaflet (see figure 5(a)). The tricuspid leaflets are modeled as hyperbolic paraboloids and implicitly describe the tricuspid annulus. Their grids are spanning along the annulus circumferential direction $\mathbf{u}$ and the perpendicular vector v pointing for the annulus towards the corresponding leaflet tip, and consist out of 22×14 vertices and 546 faces (see figure 5(b)). Each leaflet is constrained by the corresponding two commissures and one leaflet tip (see figure 5(c)).

2.4 Heart Chambers

Left Ventricle and Atrium: The left ventricle is constructed from 78 landmarks (16 mitral lateral, 15 mitral septum, 16 left ventricle output tract and 32 aortic valve control points) and four surface geometries (LV epicardium, LV endocardium and

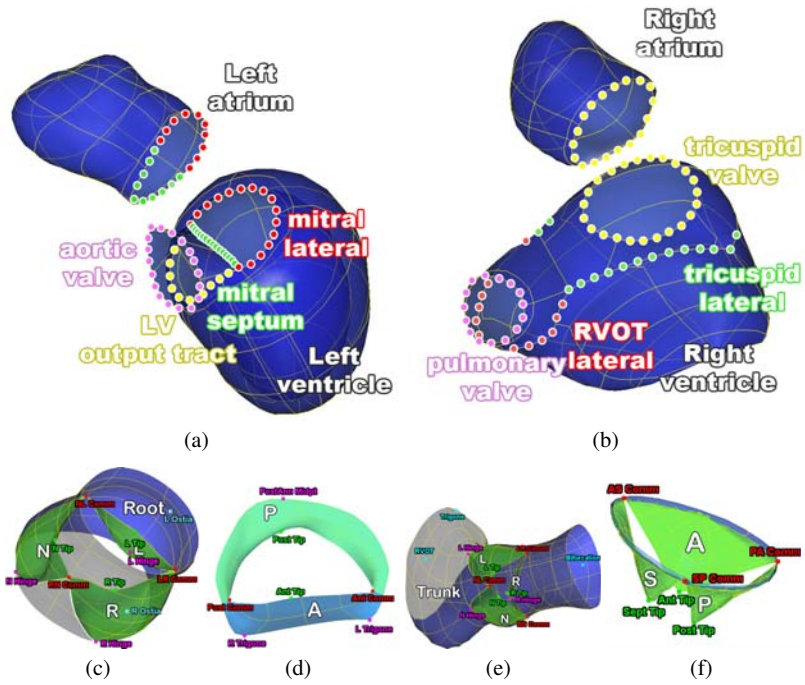

Fig. 8 Cardiac model components: (a) the left heart (left ventricle and left atrium), (b) right heart (right ventricle and right atrium), (c) aortic valve, (d) mitral valve, (e) pulmonary valve and (f) tricuspid valve.

LV output tract). The left atrial surface is connected to the left ventricle via the aortic valve control points (figure 8(a)) Zheng et al. (2008).

Right Ventricle and Atrium: The right ventricle is composed of 74 landmarks (16 tricuspid lateral, 15 tricuspid septum, 28 tricuspid valve and 18 pulmonary valve control points) and four surface geometries (RV apex, RV output tract and RV inflow tract). The right atrial surface is constrained by 28 tricuspid valve control points and links to the right ventricle (figure 8(b)) Zheng et al. (2008).

3 Parameter Estimation from Cardiac Images

3.1 Object Localization and Rigid Motion Estimation

The goal is to determine the location of each specific anatomy from multimodal cardiac images. Thus, the location and motion parameters θ of each valve, defined in section 2.1, are estimated from a sequence of volumes I:

$$\begin{aligned} &\arg\max_\theta p(\theta|I) = \arg\max_\theta \\ &p(\theta(0),\cdots,\theta(n-1)|I(0),\cdots,I(n-1)) \end{aligned} \tag{4}$$

Location Estimation: To solve equation 4, we formulate the object localization as a classification problem and estimate $\theta(t)$ for each time step t. The probability $p(\theta(t)|I(t))$ can be modeled by a learned detector D, which evaluates and scores a large number of hypotheses for $\theta(t)$. To avoid exhaustive search along a nine-dimensional space we apply the Marginal Space Learning (MSL) framework (Zheng et al. (2008)) and break the original parameter space into a subset of increasing marginal spaces:

$$\Sigma_1 \subset \Sigma_2 \subset \cdots \subset \Sigma_n = \Sigma$$

The nine-dimensional space described by the similarity transform in a three-dimensional Euclidean space is decomposed as follows:

$$\begin{aligned} \Sigma_1 &= (c_x, c_y, c_z) \\ \Sigma_2 &= (c_x, c_y, c_z, \alpha_x, \alpha_y, \alpha_z) \\ \Sigma_3 &= (c_x, c_y, c_z, \alpha_x, \alpha_y, \alpha_z, s_x, s_y, s_z) \end{aligned}$$

where Σ_1 represents the position marginal space, Σ_2 the position + orientation marginal space and Σ_3 the position + orientation + scale marginal space, which coincides with the original domain. In practice, the optimal arrangement for MSL sorts the marginal spaces in a descending order based on their variance. In our case, due to the CT, MRI and TEE acquisition protocols and physiological variations of the heart, the highest variance comes from translation followed by orientation and scale.

From the marginalization of the search domain, the target posterior probability can be expressed as:

$$\begin{aligned} &p(\theta(t)|I(t)) = p(c_x, c_y, c_z|I(t)) \\ &p(\alpha_x, \alpha_y, \alpha_z|c_x, c_y, c_z, I(t)) \\ &p(s_x, s_y, s_z|\alpha_x, \alpha_y, \alpha_z, c_x, c_y, c_z, I(t)) \end{aligned}$$

Instead of using a single detector D, we train detectors for each marginal spaces D_1, D_2 and D_3, and estimate $\theta(t)$ by gradually increasing the dimensionality. Detectors are trained using the Probabilistic Boosting Tree (Tu (2005)) with Haar and Steerable Features (Zheng et al. (2008)). After each stage only a limited number of high-probability candidates are kept to significantly reduce the search space: 100 highest score candidates are retained in Σ_1, 50 in Σ_2 and 25 in Σ_3.

Robust Motion Aggregation: $[\theta_0(0)\dots\theta_{25}(0)]\dots[\theta_0(n-1)\dots\theta_{25}(n-1)]$ are the candidates with the highest score estimated at each time step $t, t = 0,\dots n-1$. To obtain a temporally consistent global location and motion $\theta(t)$, a RANSAC estimator is employed. We assume a constant model for the cardiac motion, which drives the global movement of the entire valvular apparatus. From randomly sampled candi-

dates, the one yielding the maximum number of inliers is picked as the final motion. Inliers are considered within a distance of $\sigma = 7mm$ from the current candidate and extracted at each time step t. The distance measure $d(\theta(t)_1, \theta(t)_2)$ is given by the maximum L1 norm of the standard unit axis deformed by the parameters $\theta(t)_1$ and $\theta(t)_2$, respectively:

$$\begin{array}{ll} L1(\mathbf{a_1}, \mathbf{a_2}) & = max\{|x1-x2|, |y1-y2|, |z1-z2|\} \\ d(\theta(t)_1, \theta(t)_2) & = \frac{1}{4}(L1(\mathbf{c_1}, \mathbf{c_2}) + L1(\mathbf{X}_1 s_{x1}, \mathbf{X}_2 s_{x2}) + L1(\mathbf{Y}_1 s_{y_1}, \mathbf{Y}_2 s_{y_2}) \\ & \quad + L1(\mathbf{Z}_1 s_{z1}, \mathbf{Z}_2 s_{z2})) \end{array} \tag{5}$$

where X,Y and Z are the unit axes obtained from the Euler angles $(\alpha_x, \alpha_y, \alpha_z)$, $\mathbf{c}$ the position vectors, and s_x, s_y, s_z scale parameters.

3.2 Trajectory Spectrum Learning for Non-Rigid Motion Estimation

Based on the determined global location and rigid motion, in this section we introduce a trajectory spectrum learning algorithm to estimate non-linear landmark movements from volumetric sequences (Ionasec and et al. (2009)). Considering the representation in section 2.1 equation 2, the objective is to find for each landmark j its trajectory $\mathbf{L^j}$, with the maximum posterior probability from a series of volumes $I(t)$, given the rigid motion $\theta(t)$:

$$\begin{array}{l} \arg\max_{\mathbf{L^j}} p(\mathbf{L^j}|I, \theta) = \arg\max_{\mathbf{L^j}} p(\mathbf{L^j}(0), \cdots, \mathbf{L^j}(n-1)| \\ I(0), \cdots, I(n-1), \theta(0), \cdots, \theta(n-1)) \end{array} \tag{6}$$

It is difficult to solve Eq. 6 directly, thus various assumptions, such as the Markovian property of the motion (Yang et al. (2008)), have been proposed to the posterior distribution over $\mathbf{L^j(t)}$ given images up to time t. However, results are often not guaranteed to be smooth and may diverge over time, due to error accumulation. These fundamental issues can be addressed effectively if both, temporal and spatial appearance information is considered over the whole sequence at once. A trajectory can be uniquely represented by the concatenation of its Discrete Fourier Transform (DFT) coefficients,

$$\mathbf{s^j} = [\mathbf{s^j}(0), \mathbf{s^j}(1), \cdots, \mathbf{s^j}(n-1)] \tag{7}$$

where $\mathbf{s^j}(f) \in \mathscr{C}^3$ is the frequency spectrum of the x, y, and z components of the trajectory $\mathbf{L^j}(t)$, and $f = 0, 1, \cdots, n-1$. The magnitude of $\mathbf{s^j}(f)$ is used to describe the shift-invariant motion according to the shift theorem of DFT, while the phase information is used to handle temporal misalignment. Equation 6 can be reformulated as finding the DFT spectrum $\mathbf{s^j}$, with the maximal posterior probability:

$$\begin{aligned}&\arg\max_{\mathbf{s^j}} p(\mathbf{s^j}|I,\theta) = \arg\max_{\mathbf{s^j}} p(\mathbf{s^j}(0),\cdots,\mathbf{s^j}(n-1)|\\ &I(0),\cdots,I(n-1),\theta(0),\cdots,\theta(n-1))\end{aligned} \tag{8}$$

Instead of estimating the motion trajectory directly, we apply discriminative learning to detect the spectrum $\mathbf{s^j}$ in the frequency domain by optimizing equation 8.

Search Space Marginalization: Inspired by the MSL, we efficiently perform trajectory spectrum learning and detection in DFT subspaces with gradually increased dimensionality. The intuition is to perform a spectral coarse-to-fine motion estimation, where the detection of coarse level motion (low frequency) is incrementally refined with high frequency components representing fine deformations.

As described earlier, the motion trajectory is parameterized by the DFT spectrum components $\mathbf{s}^j(f), f = 0,\ldots,n-1$. We differentiate between two types of subspaces, individual component subspaces $\Sigma^{(k)}$ and marginalized subspaces Σ_k defined as:

$$\Sigma^{(k)} = \{\mathbf{s}(k)\} \tag{9}$$

$$\Sigma_k = \Sigma_{k-1} \times \Sigma^{(k)} \tag{10}$$

$$\Sigma_0 \subset \Sigma_1 \subset \ldots \subset \Sigma_{r-1}, r = |\zeta| \tag{11}$$

The subspaces $\Sigma^{(k)}$ are efficiently represented by a set of corresponding hypotheses $\mathscr{H}^{(k)}$ obtained from the training set. The pruned search space enables efficient learning and optimization:

$$\Sigma_{r-1} = \mathscr{H}^{(0)} \times \mathscr{H}^{(1)} \times \ldots \times \mathscr{H}^{(r-1)}, r = |\zeta|$$

Learning in Marginal Trajectory Spaces: The algorithm starts by learning the posterior probability distribution in the DC marginal space Σ_0. Subsequently, the learned detector D_0 is applied to identify high probable candidates $\mathscr{C}_0$ from the hypotheses $\mathscr{H}^{(0)}$. In the following step, the dimensionality of the space is increased by adding the next spectrum component (in this case the fundamental frequency, $\Sigma^{(1)}$). Learning is performed in the restricted space defined by the extracted high probability regions and hypotheses set $\mathscr{C}_0 \times \mathscr{H}^{(1)}$. The same operation is repeated until reaching the genuine search space Σ_{r-1}.

For each marginal space Σ_k, corresponding discriminative classifiers D_k are trained on sets of positives Pos_k and negatives Neg_k. We analyze samples constructed from high probability candidates $\mathscr{C}_{k-1}$ and hypotheses $\mathscr{H}^{(k)}$. The sample set $\mathscr{C}_{k-1} \times \mathscr{H}^{(k)}$ is separated into positive and negative examples by comparing the corresponding trajectories to the ground truth in the spatial domain using the following distance measure:

$$d(\mathbf{L^j}_1, \mathbf{L^j}_2) = \max_t \|\mathbf{L^j}_1(t) - \mathbf{L^j}_2(t)\| \tag{12}$$

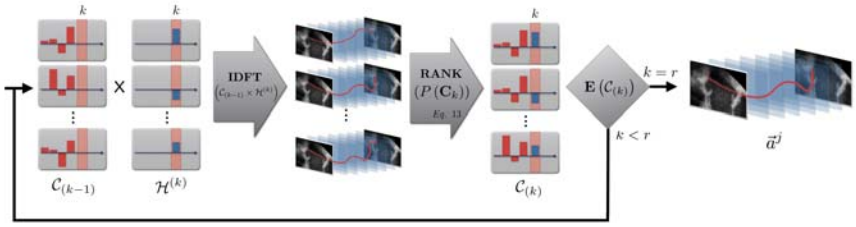

Fig. 9 Diagram depicting the estimation of non-rigid landmark motion using trajectory spectrum learning.

where $\mathbf{L^j}_1$ and $\mathbf{L^j}_2$ denote two trajectories for the j-th landmark. Positives are in a certain distance $dist_{pos}$ (e.g. 1.5mm) to the ground-truth over the whole trajectories. Negatives, however, are selected individually for each time step, if the tested position in space and time is larger than $dist_{neg}$ (e.g. 3.5mm). The probabilistic boosting tree PBT is applied to train a strong classifier D_k.

Motion Trajectory Estimation: The local non-rigid motion is parameterized by both magnitude and phase of the trajectory spectrum $\mathbf{s}^j(f)$. The parameter estimation is conducted in the marginalized search spaces $\Sigma_0,\ldots,\Sigma_{r-1}$ using the trained spectrum detectors $D_0,\ldots,D_{r-1}$ as illustrated in figure 9. Starting from an initial zero-spectrum, we incrementally estimate the magnitude and phase of each frequency component $\mathbf{s}(k)$. At the stage k, the corresponding robust classifier D_k is exhaustively scanned over the potential candidates $\mathscr{C}_{k-1}\times\mathscr{H}^{(k)}$. The probability of a candidate $\mathbf{C_k}\in\mathscr{C}_{k-1}\times\mathscr{H}^{(k)}$ is computed by the following objective function:

$$p(\mathbf{C_k})=\prod_{t=0}^{n-1}D_k(IDFT(\mathbf{C_k}),I,t) \tag{13}$$

where $t=0,\ldots,n-1$ is the time instance (frame index). After each step k, the top 50 trajectory candidates $\mathscr{C}_k$ with high probability values are preserved for the next step $k+1$. The procedure is repeated until a final set of trajectory candidates $\mathscr{C}_{r-1}$, defined in the full space Σ_{r-1}, is computed.

3.3 Comprehensive Model Estimation

The final stage in our hierarchical model estimation algorithm is the delineation of the full morphology and dynamics of the anatomies:

$$\begin{aligned}&\arg\max_M p(M|I,\theta,\mathbf{L})=\arg\max_M p(M(0),\cdots,M(n-1)|\\&I(0),\cdots,I(n-1),\theta(0),\cdots,\theta(n-1),\mathbf{L}(0),\cdots\mathbf{L}(n-1))\end{aligned} \tag{14}$$

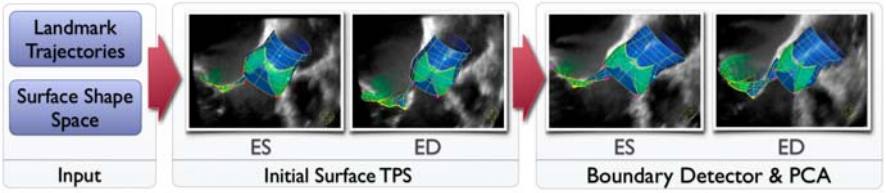

Fig. 10 Diagram depicting the estimation of the comprehensive valve model. Estimation in cardiac key phases, end-diastole and end-systole.

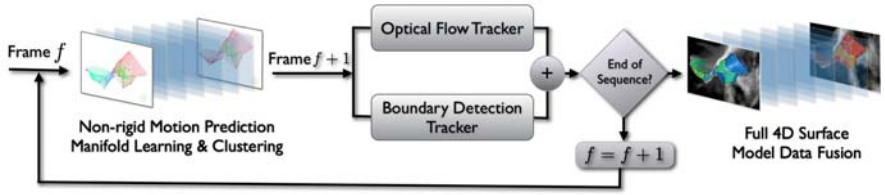

Fig. 11 Diagram depicting the estimation of the comprehensive valve model. Estimation in the full cardiac cycle.

The shape model is first estimated in the End-Diastole (ED) and End-Systole (ES) phases of the cardiac cycle and then the non-rigid deformation is propagated to the remaining phases using a learned motion prior.

Estimation in Cardiac Key Phases: Using the previously estimated model parameters, a pre-computed mean shape of the comprehensive valvular model is placed into the volumes $I(t_{ED})$ and $I(t_{ES})$ through a TPS transform Bookstein (1989). The initial estimate is then deformed to fit the true valvular anatomy using learned object boundary detectors, regularized by statistical shape models (see figure 10).

Learning based methods provide robust results Zheng et al. (2008); Yang et al. (2008) by utilizing both gradients and image intensities at different image resolutions and by incorporating the local context. Hence, the non-rigid deformation is guided by a boundary detector D_b learned using the probabilistic boosting-tree and steerable features (Zheng et al. (2008)). After initialization, D_b evaluates hypotheses for each discrete boundary point along its corresponding normal direction. The new boundary points are set to the hypotheses with maximal probability. To guarantee physiologically compliant results, the final model is obtained after projecting the estimated points to the statistical shape space (Ionasec et al. (2010)).

Motion Estimation: Starting from the detection results in the ED and ES phases, the model deformations are propagated in both forward and backward directions using learned motion priors similar as in Yang et al. (2008) (see figure 11). The motion prior is estimated at the training stage using motion manifold learning and hierar-

chical K-means clustering, from a pre-annotated database of sequences containing one cardiac cycle each. First the temporal deformations are aligned by 4D generalized procrustes analysis. Next a low-dimensional embedding is computed from the aligned training sequences using the ISOMAP algorithm Tenenbaum et al. (2000), to represent the highly nonlinear motion of the heart valves. Finally, in order to extract the modes of motion $\overline{\mathbf{X}}_m$, the motion sequences are clustered with hierarchical K-means based on the Euclidean distance in the lower dimensional manifold.

One-step forward prediction is used to select the correct motion mode for predicting time step T. Therefore the previous shapes $M(t)$ from time steps $t = 1 \cdots T-1$ and the corresponding time steps in each of the motion modes $\overline{\mathbf{X}}_m$ are sub-sampled by a constant factor k and the TPS transform T_{TPS} computed. The mean error between the warped shape and the corresponding shape on each motion mode is computed, and the motion mode with minimum distance is selected for prediction:

$$E_{TPS}(\overline{\mathbf{X}}_m(t), M(t)) = \frac{k}{N} \sum_{j=1}^{N/k} ||{\overline{\mathbf{X}}_m}^j(t) - T_{TPS}(M^j(t))|| \tag{15}$$

$$\overline{\mathbf{X}}(T) = \arg\min_m \frac{1}{T-1} \sum_{t=1}^{T-1} E_{TPS}(\overline{\mathbf{X}}_m(t), M(t)) \tag{16}$$

where N denotes the number of points in $M(t)$, ${\overline{\mathbf{X}}_m}^j$ and M^j are shape vertices, and $\overline{\mathbf{X}}(T)$ the selected motion mode. The shape prediction $M(T)'$ for the following frame T is then computed by inverse TPS mapping $M(T)' = T_{TPS}^{-1}(\overline{\mathbf{X}}(T))$ and the boundary detector D_b deforms the initialization to make it fit the data in the update step. To ensure temporal consistency and smooth motion and to avoid drifting and outliers, two collaborative trackers, an optical flow tracker and a boundary detection tracker D_b, are used in our method. The results are then fused into a single estimate by averaging the computed deformations and the procedure is repeated until the full 4D model is estimated for the complete sequence.

3.4 Regression-based Surface Reconstruction

Sections 3.1 - 3.3 describe the framework for parameter estimation from dense 4D images. In this section we present a regression-based method for estimating model parameters from sparse 4D data, usually produced during Cardiac Magnetic Resonance (CMR) exams.

In *regression* a solution to the following optimization problem is normally sought Zhou et al. (2005):

$$\hat{\mathscr{R}}(\mathbf{x}) = argmin_{\mathscr{R} \in \mathfrak{I}} \sum_{n=1}^{N} L\left(y(\mathbf{x}_n), \mathscr{R}(\mathbf{x}_n)\right)/N \tag{17}$$

where $\Im$ is the set of possible regression functions, $L(\circ,\circ)$ is a loss function that penalizes the deviation of the regressor output $\mathscr{R}(\mathbf{x}_n)$ from the true output, and N is the number of available training examples. In our case the reconstruction task is defined as a regression problem between the full surface model of a heart valve and the respective sparse data acquired using the proposed CMR protocol:

$$\mathbf{M} = \hat{\mathscr{R}}(\mathbf{x}_{sparse})) + \varepsilon \tag{18}$$

In our regression problem both for input and output data we focus on shape information and ignore respective volume data. Thus, the output M is always a set of m 3D points as defined in section 2.1.

Invariant Shape Descriptors: The input, $\mathbf{x}_{sparse}$, are shape descriptors (SD) describing the cloud of points belonging to surface in the sparse CMR data. The simplest but reliable solution is to use the coordinates of known points as input Vitanovski et al. (2010). A different solution, which we exploit here, is to use angles, distances and areas between random sampled points as point cloud descriptors Osada et al. (2002):

- ***A3:*** Measures the Angle between three random points;
- ***D2:*** Measure the distance between two random points;
- ***D3:*** Measures the square root of the area of the triangle between three random points;

For the different shape descriptors proposed by Osada et al. (2002) we measured feature importance by analysing the features selected by additive boosting. We have identified (A3, D2 and D3) to be most informative in our context with the average probability of occurrence 0.11, 0.07, and 0.13, correspondingly. In addition, all three types are translation, rotation and scale invariant descriptors which overcome the necessity of point correspondences. Finally, histogram bins and the four first normalized central moments describing the histogram distribution are computed from the descriptors and incorporate in the regression model as input.

Ensembles of Additive Boosting Regressors: Each component m regression problem $\hat{\mathscr{R}}^m$ is solved by learning using additive boosting regression (ABR) Friedman (2000). In ABR, the weak regressors ρ_t are sequentially fit to the residuals, starting from the mean $\overline{M}$ and proceeding with the residuals of the availabe set of weak regressors themselves. In ABR, the output function is assumed to take a linear form as follows Friedman (2000):

$$\hat{\mathscr{R}}(\mathbf{x}) = \sum_{t=1}^{T} \alpha_t \rho_t(\mathbf{x}); \rho_t(\mathbf{x}) \in \Im \tag{19}$$

where $\rho_t(\mathbf{x})$ is a base (weak) learner and T is the number of boosting iterations.

We use very simple weak regressors as the base learners: ***simple 1D linear regression*** (SLR), ***logistic stumps*** (LS) and ***decision stumps*** (DS). For SLR, in each

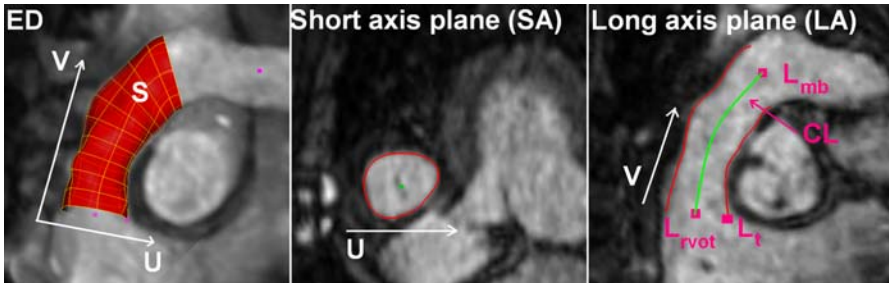

Fig. 12 Left: 3D MRI scan of the whole heart in the ED phase. **Middle:** short axis imaging plane. **Right:** long axis imaging plane

boosting iteration a feature which results in the smallest squared loss with linear regression is added to the pool of already selected features. Each weak learner is thus a simple linear regressor of the form ($y = \beta_1 x + \beta_0$) where x is the selected shape descriptor and y is a scalar output coordinate. LS is a simple logistic function on one shape descriptor x:

$$y = \frac{1}{1+e^{-z}}, z = \beta_1 x + \beta_0 \tag{20}$$

Finally, DS is a piecewise linear threshold function where threshold θ is selected so that the variance in the subsets of instances produced is minimized. Generalization performance improvement of the underlying regression models and avoidance of overfitting is achieved by injecting randomization in the input data and random features sub spacing (BRFS), similar to Webb (2000). In particular, instead of providing a single model $\mathscr{R}$ for the training set X, we generate a set of models $\mathscr{R}_i^j$, each obtained using the same additive regression procedure but on a *random sample* of the data, with instances S_i obtained using random sampling with replacement, and a subset of features F_j including 50% features randomly sampled without replacement from the original set. The final solution is then simply the mean surface for the surfaces obtained with the regressors generated from the random samples:

$$\mathscr{R} = mean_{i,m}(\mathscr{R}_i^m) \tag{21}$$

Regression-based Pulmonary Valve Model Estimation from 2D+t CMR: In clinical settings the long acquisition time characteristic to CMR is reduced by scanning the Pulmonary Valve (PV) with a sparse 4D CMR protocol. Thus, one end-diastolic 3D volume I_{ED} and two orthogonal 2D+t cine images, short axis (SA) and long axis (LA) (see figure 12) instead of a dense 4D image. We apply the regression-based surface reconstruction to estimate a 4D patient-specific model of the pulmonary valve $M_{pulmonary}$ from the sparse data:

$$M_{pulmonary} = \mathscr{R}(SD[M(t_{ED}), (C_{LA}, C_{SA})_{1...T}]) \tag{22}$$

where $M(t_{ED})$ is the pulmonary valve model in I_{ED} and $(C_{LA}, C_{SA})_{1...T}$ the pulmonary valve contours in the LA and SA images over the entire sequence of length T. $M(t_{ED}), (C_{LA}, C_{SA})_{1...T}$ are estimated using the pipeline from section 3.1 - 3.3. The method is similarly applied to estimate other anatomical structures from sparse images.

4 Experimental Results

In this section we demonstrate the performance of the proposed patient-specific parameter estimation framework from multi-modal images. Experiments are performed on a large and heterogeneous data set acquired using CT, TEE and MRI scanners from 476 patients affected by a large spectrum of cardiovascular and valvular heart diseases: regurgitation, stenosis, prolapse, aortic root dilation, bicuspid aortic valve and Tetralogy of Fallot. The imaging data set includes 1330 cardiac CT, 5061 TEE and 83 CMR volumes, which were collected from medical centers around the world.

Each volume in our data set is associated with an annotation obtained through an expert-guided process that includes the manual placing of anatomical landmarks and delineation of anatomical surfaces. The obtained models are consider as ground truth and were used for training and testing of the proposed algorithms. Three-fold cross validation was performed for all experiments and reported results reflect performance on unseen, test data.

Performance of the Object Localization and Rigid Motion Estimation: The performance of the global location and rigid motion estimation, θ, described in section 3.1 is quantified at the box corners of the detected time-depenedent similarity transformation. The average Euclidean distance between the eight bounding box points, defined by the similarity transform parameters $\{(c_x, c_y, c_z), (\alpha_x, \alpha_y, \alpha_z), (s_x, s_y, s_z), t\}$ and the ground-truth box is reported. Table 1 illustrates the mean errors and corresponding standard deviations distributed over the four valves and employed image modalities. The average accuracy of the individual detection stages is $3.09 \pm 3.02mm$ for position, 9.72 ± 5.98 for orientation, and 6.50 ± 4.19 for scale.

Mean / STD (mm)	Aortic Valve	Mitral Valve	Pulmonary Valve	Tricuspid Valve
TEE	4.78±3.26	5.00±2.02	-	-
Cardiac CT	4.40±1.98	6.94±2.19	7.72±10.03	-
CMR	-	-	7.19±3.50	-

Table 1 Accuracy of the global location and rigid motion estimation, quantified from the box corners and reported using the mean error and standard deviation distribution over each valve and employed modality.

Performance of the Non-Rigid-Landmark Motion Estimation: The accuracy of the Trajectory Spectrum Learning algorithm (see section 3.2), which estimate the non-rigid landmark motion model, L, is measured using the Euclidean distance between detected and corresponding ground truth landmark trajectories. Table 2 demonstrates the precision expressed in mean errors and standard deviations, distributed over the four valves and three data sources. Note that reported values are obtained by averaging the performance of individual landmarks with respect to the corresponding valve.

Mean / STD (mm)	Aortic Valve	Mitral Valve	Pulmonary Valve	Tricuspid Valve
TEE	2.79±1.26	3.60±1.56	-	-
Cardiac CT	2.72±1.52	2.79±1.20	3.50±2.70	-
CMR	-	-	4.30±3.00	-

Table 2 Accuracy of the non-rigid landmark motion estimation, quantified by the Euclidean distance and reported using the mean error and standard deviation distribution over each valve and employed modality.

Performance of the Comprehensive Valve Model Estimation: The accuracy of the comprehensive valvular model estimation, M, (see section 3.3) is evaluated by utilizing the point-to-mesh distance. For each point on a surface $\mathbf{p}$, we search for the closest point (not necessarily one of the vertices) on the other surface to calculate the Euclidean distance. To guarantee a symmetric measurement, the point-to-mesh distance is calculated in two directions, from detected to ground truth surfaces and vice versa. Tabel 3 contains the mean error and standard deviation distributed over the four valves and image types. Examples of estimation results are given in figure 13.

Mean / STD (mm)	Aortic Valve	Mitral Valve	Pulmonary Valve	Tricuspid Valve
TEE	1.35±0.54	2.29±0.64	-	-
Cardiac CT	1.22±0.38	2.02±0.57	1.60±0.20	-
CMR	-	-	1.90±0.20	-

Table 3 Accuracy of the comprehensive valve model estimation, quantified by the Point-to-Mesh distance and reported using the mean error and standard deviation distribution over each valve and employed modality.

Overall, the estimation accuracy of the patient-specific valvular parameters from multi-modal images is 1.73mm. On a standard PC with a quad-core 3.2GHz processor and 2.0GB memory, the total computation time for the all three estimation stages is 4.8 seconds per volume (approx 120sec for average length volume sequences), from which the global location and rigid motion estimation requires 15%

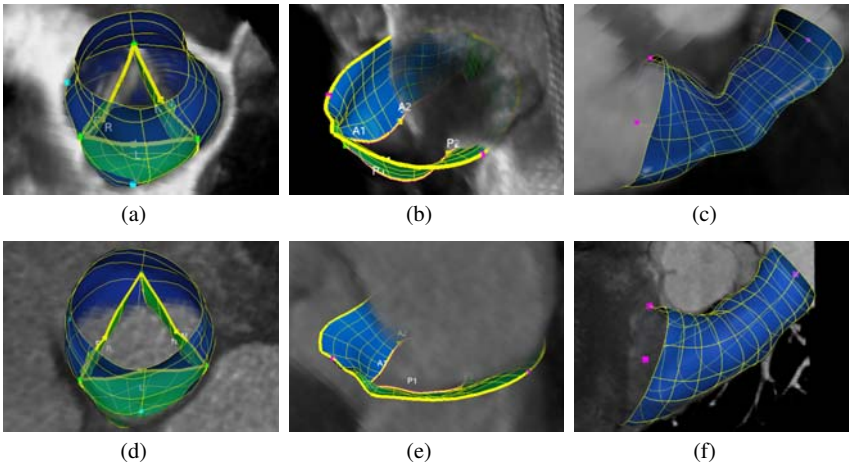

Fig. 13 Examples of comprehensive valves model estimation: (a) aortic valve in TEE, (b) mitral valve in TEE, (c) pulmonary valve in CMR, (d) aortic valve in cardiac CT, (e) mitral valve in cardiac CT, and (f) pulmonary valve in cardiac CT.

of the computation time (approx 0.7sec), non-rigid landmark motion 54% (approx 2.6sec), and comprehensive valvular estimation 31% (approx 1.5sec).

5 Clinical Applications

5.1 Valve Analysis for Transcatheter Aortic Valve Implantation

It is axiomatic that precise quantification of the anatomy and function is fundamental in the medical management of valvular heart disease. Emerging percutaneous and minimally invasive valve interventions, such as the Transcatheter Aortic Valve Implantation (TAVI), require extensive non-invasive assessment, as clinicians have restricted direct access to the sensitive anatomies (Akhtar et al. (2009); Piazza et al. (2008)). Measurements of the aortic annulus are mandatory for the correct sizing the prosthetic implant, while precise knowledge of the coronary ostia position prevents hazardous ischemic complications by avoiding the potential misplacement of aortic valve implants. Data about the integral three-dimensional configuration of critical structures (ostia, commissures, hinges, etc.) and their relative location over the entire cardiac cycle becomes increasingly relevant.

We proposed a paradigm shift in the clinical evaluation of the valvular apparatus, which replaces manual analysis based on 2D images with automated model-based quantification from 4D data. At the center of the proposed approach is the dynamic valvular model introduced in section 2, which captures comprehensive

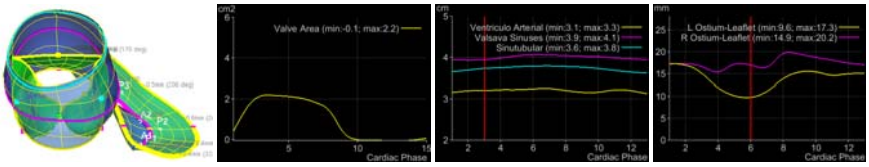

(a)

Fig. 14 Examples of aortic-mitral morphological and functional measurements. From left to right: aortic valve model with measurement traces, aortic valve area, aortic root diameters and ostia to leaflets distances.

patient-specific information of the morphology and functions from multi-modal images following the methods described in section 3. The explicit mathematical model is exploited to express a wide-ranging collection of quantitative parameters that support the overall clinical decision making process (see figure 14). In comparison with the gold standard, which processes 2D images and performs manual measurements, the key benefits of the proposed model-based analysis are: increased precision and reproducibility, decreased processing time, and integrated and comprehensive analysis. In the following we present a series of clinical validation experiments performed jointly with various clinical collaborators (Calleja et al. (2010); Gassner et al. (2008); Ionasec et al. (2008a); Choi et al. (2008)).

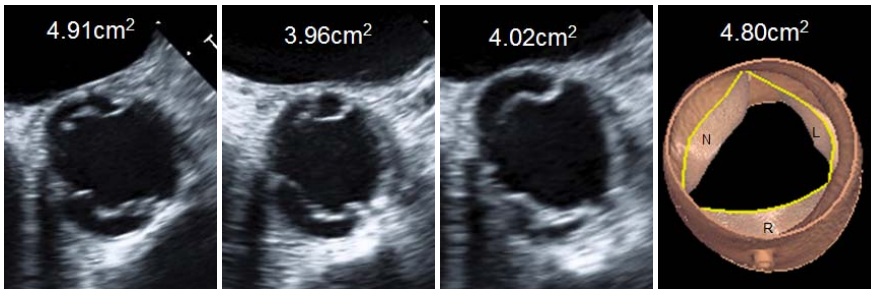

(a) (b) (c) (d)

Fig. 15 Aortic Valve Area measured manually from 2D images versus the automatic 3D model-based quantification: (a), (b) and (c) show the manual measurement from three different 2D TEE images of the same patient, which demonstrate the sensitivity of the current gold standard approach to the position of the 2D-dimensional section. (d) shows the proposed precise and reproducible 3D model-based measurement.

Aortic Valve Opening Area Analysis from cardiac CT: The usefulness of cardiac CT to assess the aortic valve opening area (AVA) has been exhaustively documented Halpern (2008). However, manual valve planimetry is cumbersome and time-consuming. In the following experiment we evaluated the accuracy and time-effectiveness of automated model-based AVA computation compared to manual planimetry. Retrospectively ECG-gated cardiac CT data of 32 patients scanned

with dual-source CT (n=21) or 64-slice CT (n=11) were included. Data were reconstructed at 10% increments across the cardiac cycle with 1.5mm section thickness and 1mm increment. Two independent observers performed manual planimetric measurements by tracing the maximal systolic orifice on double oblique short axis multiplanar reconstructions. The same data were then analyzed using an automatic model-based method. The leaflets' geometries during maximal opening define the course of the free margins. The encompassed AVA can be computed as a surface integral.

Data was analyzed using linear regression and Bland Altman plots. Interobserver and intermethod variances were calculated. Analysis times for both methods were recorded. Mean AVA by CT planimetry was $3.62 \pm 1.21 cm^2$. Mean AVA derived from the model was $3.74 \pm 1.34 cm^2$. Excellent correlation was found between planimetric and automated quantification (r=0.963, p¡0.0001). Bland Altman plots revealed a systematic bias of $0.12 \pm 0.38 cm^2$. Intermethod variance did not differ significantly from interobserver variance (0.28 vs $0.25 cm^2$), placing 82% of model measurements between user measurements. Mean analysis time was significantly reduced for model-based measurements (mean 125sec), compared with manual planimetry (mean 230sec). The proposed model-based method allows automated, patient specific morphologic and dynamic quantification of AVA. Measurement results are within the interobserver variance of manual planimetry. Quantification of AVA derived from an aortic valve model enables fast, accurate assessment in excellent agreement with manual planimetry and has the potential to improve cardiac imaging workflow.

Aortic Valve and Root Analysis from cardiac CT and 3D TEE: Accurate anatomical and functional assessment of AV and aortic root is crucial for understanding the pathophysiology of abnormalities and for managemening decision-making in patient with aortic valve disease and aortic aneurysm. The aim of this study was to evaluate the feasibility of the modal-based method to assess the aortic valve and aortic root from volumetric 3-D Echo compared to CT. Volume-rendered 3-D TEE data were obtained using V5M transducer, Siemens Sequoia. Volumetric CT images were acquired using 64-Slice CT(Avanto, Siemens). We dynamically measured the AVA(cm2), diameter of sinotubular junction(d-STJ, mm), sinus of Valsalva(d-SV, mm) and basal ring(d-BR, mm). 364 CT volumes from 41 patients and 23, 3-D TEE volumes from 15 patients with normal to mild AR were acquired. 3-D TEE data about AV and root showed strong correlation with CT data, as illustrated in table 5.1. This novel automated model-based approach provides accurate dimensions of the AV and the aortic root and may aid in valve and root repair procedures (see figure 15).

Aortic Valve and Root in Aortic Regurgitation from 3D TEE: In this study we applied the model-based analysis approach to automatically quantify the aortic valve and the root from 3-D TEE data in patients with aortic regurgitation (AR). Volumetric 3-D TEE of the AV and proximal root from 15 patients with AR was analyzed. The conventional measures were compared to 2-D, and the non-conventional mea-

	3D TEE	cardiac CT	r-value	p-value
AVA (cm^2)	3.09 ± 0.85	4.33 ± 1.36	0.707	0.013
Max. Ventriculoarterial Junct. $\oslash$ (mm)	2.42 ± 0.27	2.74 ± 0.36	0.982	0.018
Max. Valsava Sinuses $\oslash$ (mm)	3.16 ± 0.32	3.92 ± 0.46	0.993	0.007
Max.Sinotubular Junct. $\oslash$ (mm)	2.69 ± 0.26	3.19 ± 0.21	0.775	0.042

Table 4 Comparison of AVA and aortic diameter between cardiac CT and 3D TEE

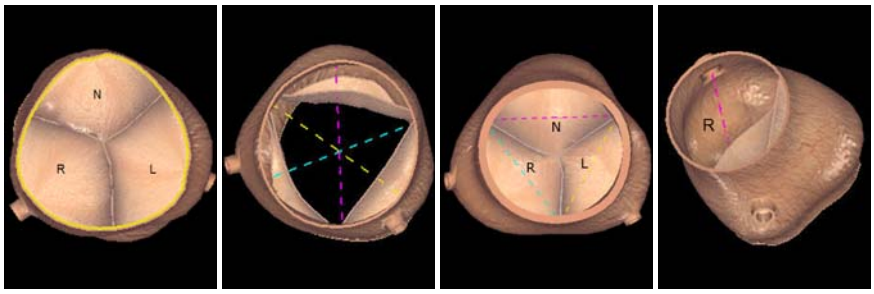

(a) (b) (c) (d)

Fig. 16 Examples of model-based aortic valve measurements: (a) aortic annular diameter (ventriculoarterial junction), (b) sinus width, (c) inter-commissural distances, and (d) coronary ostia to leaflet tip distances.

sures were compared to known normal database. Conventional measures- 2-D and the model-based measures of AV area (r=0.98), STJ diameter (r=0.73) and SV diameter (r=0.79) showed good correlation; annular diameter was discordant (r=0.58) consistent with its complex geometry in AR. Nonconventional measures (abnormal vs. normal, mm) by the model-based method - Inter-commissural distance (mm) was increased (Left: 25.9+3 Vs. 25, Right: 27.1+3 Vs. 25.9 and Non: 27.2+3 Vs. 25.5), Annulus to coronary ostia distance (mm) was increased (Right: 19.3+3 Vs. 17.2+3 and Left 16.9+3 Vs. 14.4+3); also, leaflet tip to ostia minimum distance was 5+1.6 (R) and 8+1.2 (L). The directly measured 3-D ERO in mild AR was $10-20mm^2$ and moderate AR was $30mm^2$. Automated quantification of the aortic and the root yields vital and incremental measures which may be valuable to guide surgical and percutaneous interventions to improve outcomes.

5.2 Patient Selection for Percutaneous Pulmonary Valve Implantation

Until recently, pulmonary valve replacement has been exclusively performed trough open heart surgery Boudjemline MD et al. (2004), with all associated risks: high morbidity, incidence of neurological damage, stroke and repeated valve replacement Parr et al. (1977). Novel Percutaneous Pulmonary Valve Implantation (PPVI)

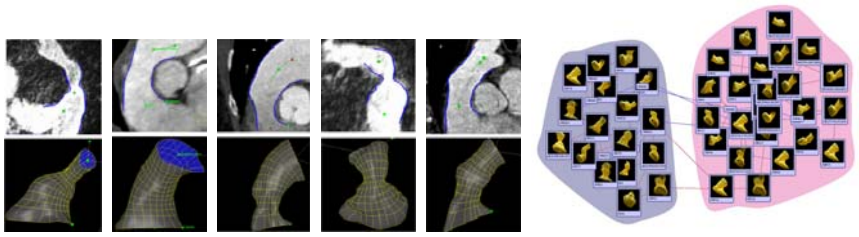

Fig. 17 Types of pulmonary trunk morphologies: (a) pyramidal shape, (b) constant diameter, (c) inverted pyramidal shape, (d) narrowed centrally but wide proximally and distally, (e) wide centrally but narrowed proximally and distally Schievano et al. (2007a). (f) Relative neighborhood graph with unsuitable (blue cluster) and suitable (red cluster) individuals.

techniques Schievano et al. (2007c), offer a less traumatic and safer treatment of the pulmonary valve Carnaghan (2006).

The selection of patient for PPVI treatment is largely based on the morphology of the pulmonary trunk Bonhoeffer et al. (2002). Intervention in unsuitable anatomies exposes patients to unnecessary invasive catherization, for which the implanted device has a high probability of proximal device dislodgment. In an effort to standardize the selection process, Schievano et al. (2007a) proposed a classification of various morphologies, based on geometric measures and appearance of the right-ventricular outflow tract and the pulmonary trunk, into five groups: pyramidal shape (type I), constant diameter (type II), inverted pyramidal shape (type III), wide centrally but narrowed proximally and distally (type IV), and narrowed centrally but wide proximally and distally (type V) (see figure 17). Patients from type I are considered to be unsuitable for PPVI due to the narrow artery and high probability of device migration. Therefore the main challenge lies in discriminating anatomies of type I from other four classes.

We propose a discriminative distance function learned using Random Forest in the product space to provide automated patient selection, namely classification of the subjects into two classes: PPVI suitable and PPVI unsuitable (see figure 17(f)). We formulate the problem as follows:

$$\hat{y} = \underbrace{argmax}_{y \in \{-1,+1\}} \left(p(y|C)\right) \quad C = (\mathbf{p}_0, \cdots, \mathbf{p}_N, F_0, \cdots, F_Q) \tag{23}$$

where $y \in \{-1,+1\}$ are the application specific labels and each model instance is represented by a parameter vector C, composed out of N surface vertices $\mathbf{p}_i \in M_{pulmonary}$ (see Section 2) and Q application dependent features F_i derived from the model. Instead of learning directly the posterior probability, a distance learning followed by the actual classification is performed, where each step requires search in a less complex functional space than in the immediate learning Tsymbal et al. (2010). Thus, learning is performed from weak representations described through equiva-

lence constraints (C^1, C^2, y), where C^1 and C^2 are feature vectors (see Equation. 23) and $y \in \{+1, -1\}$ is a label indicating whether the two instances are similar or dissimilar Hertz (2006). Using Random Forest (RF) for the learning algorithm, for a given forest f the similarity between two instances C^1 and C^2 is calculated as follows: 1) the instances are propagated down all K trees within f and their terminal positions z in each of the trees ($z_1 = (z_{11}, \cdots, z_{1K})$ for C^1, similarly z_2 for C^2) are recorded, and 2) the similarity between the two instances then equals to (I is the indicator function):

$$S(C^1, C^2) = \frac{1}{K} \sum_{i=1}^{K} I(z_{1i} = z_{2i}) \tag{24}$$

The proposed automated PPVI patient selection method was evaluated on a population of 102 patients that include all five types of pulmonary trunk geometry (figure 17) and cumulated into 50 patient of type I (i.e. unsuitable for PPVI) and 52 patients with suitable geometries. The accuracy of methods is validated by leave-one-out cross-validation for various classification approaches including k-Nearest Neighbors (kNN), AdaBoost (AB) and Random Forests (RF) in the canonical space, as well as AdaBoost and Random Forests[23] in the product and difference spaces (AB-pr, RF-pr, AB-di and RF-di) and intrinsic RF distance (RF-dist). AdaBoost in the product space showed highest performance for the PPVI suitability selection with 91% correct classification. The proposed approach has the potential to significantly improve accuracy and reproducibility of patient selection for PPVI and pre-procedural PPVI planning.

6 Conclusion

The main subject addressed in this chapter is the patient-specific estimation of physiological heart valvular and chamber models from multi-modal cardiac images. We proposed a physiological model of the heart valves to precisely capture their anatomical, dynamical and pathological variations. Our model is hierarchically defined and comprehensively represents the location and rigid motion, anatomical landmarks and the comprehensive shape and dynamics of all four cardiac valves: aortic, mitral, tricuspid and pulmonary valves. We presented discriminative learning-based framework that permits the estimation of patient-specific model parameters from cardiac images. In the first step Marginal Space Learning and RANdom SAmple Consensus are applied for the time-coherent detection of the valvular location and motion from an arbitrary four-dimensional cardiac scan. Subsequently, Trajectory Spectrum Learning robustly estimates the parameters of the anatomical landmarks from four-dimensional image sequences. The last method performs object delineation of dynamic models, using boundary detectors and motion manifold learning techniques. The performance of the proposed estimation framework is demonstrated through extensive experiments on 476 patients, which results into an average precision of 1.73mm and speed of 4.8 seconds per volume. Two clinical applications based on

the modeling and estimation techniques are described: a novel paradigm for the clinical analysis of the valvular apparatus with application to Transcatheter Aortic Valve Implantation, and automated patient selection method for Percutaneous Pulmonary Valve Implantation based on learning-based distance functions. The technology described in this chapter can potentially advance the management of patients affected by valvular heart disease by reducing clinical investigation costs, risks for complications during procedures, and ultimately by improving the overall outcome of valvular treatment.

References

Agarwal, A., Triggs, B., 2004. Tracking articulated motion using a mixture of autoregressive models, in: Proc. European Conf. Computer Vision, pp. III 54–65.

Akhtar, M., Tuzcu, E.M., Kapadia, S.R., Svensson, L.G., Greenberg, R.K., Roselli, E.E., Halliburton, S., Kurra, V., Schoenhagen, P., Sola, S., 2009. Aortic root morphology in patients undergoing percutaneous aortic valve replacement: Evidence of aortic root remodeling. The Journal of Thoracic and Cardiovascular Surgery 137, 950 – 956.

Bonhoeffer, P., Boudjemline, S.A., Qureshi, Y., Bidois, J.L., Iserin, L., Acar, P., Merckx, J., Kachaner, J., Sidi, D., 2002. Percutaneous insertion of the pulmonary valve. Journal of the American College of Cardiology 39, 1664–1669.

Bonow, R.O., Carabello, B.A., Chatterjee, K., de Leon, A.C.J., Faxon, D.P., Freed, M.D., Gaasch, W.H., Lytle, B.W., Nishimura, R.A., O'Gara, P.T., O'Rourke, R.A., Otto, C.M., Shah, P.M., Shanewise, J.S., 2006. Acc/aha 2006 guidelines for the management of patients with valvular heart disease: a report of the american college of cardiology/american heart association task force on practice guidelines (writing committee to develop guidelines for the management of patients with valvular heart disease). Circulation 114, 84–231.

Bookstein, F.L., 1989. Principal warps: Thin-plate splines and the decomposition of deformations. IEEE Transactions on Pattern Analysis and Machine Intelligence 11, 567–585.

Boudjemline MD, Y., Agnoletti MD, G., Bonnet MD, D., Sidi MD, D., Bonhoeffer MD, P., 2004. Percutaneous pulmonary valve replacement in a large right ventricular outflow tract: An experimental study. American College of Cardiology 43, 1082–1087.

Calleja, A., Razvan, I., Houle, H., Liu, S., Dickerson, J., Thavendiranathan, P., Sai-Sudhakar, C., Crestanello, J., Ryan, T., Vannan, M., 2010. Automated quantitative modeling of the aortic valve and root in aortic regurgitation using volume 3-d transesophageal echocardiography, in: American College of Cardiology Annual Meeting - ACC 2010, Atlanta, USA.

Carnaghan, H., 2006. Percutaneous pulmonary valve implantation and the future of replacement. Science and Technology 20, 319–322.

Choi, J.H., Georgescu, B., Ionasec, R.I., Raman, S., Hong, G.R., Liu, S., Houle, H., Vannan, M.A., 2008. Novel semi-automatic quantitative assessment of the aortic valve and aortic root from volumetric 3d echocardiography: Comparison to volumetric cardiac computed tomography (ct), in: AHA, New Orleans, USA.

Conti, C., Stevanella, M., Maffessanti, F., Trunfio, S., Votta, E., Roghi, A., Parodi, O., Caiani, E., Redaelli, A., 2010. Mitral valve modelling in ischemic patients: Finite element analysis from cardiac magnetic resonance imaginge, in: Computing in Cardiology.

De Hart, J., Peters, G., Schreurs, P., Baaijens, F., 2002. A three-dimensional computational analysis of fluidstructure interaction in the aortic valve. Journal of Biomechanics 36, 103–10.

Ecabert, O., Peters, J., Schramm, H., Lorenz, C., von Berg, J., Walker, M.J., Vembar, M., Olszewski, M.E., Subramanyan, K., Lavi, G., Weese, J., 2008. Automatic Model-Based Segmentation of the Heart in CT Images. IEEE Transactions on Medical Imaging 27, 1189–1201.

Friedman, J.H., 2000. Greedy function approximation: A gradient boosting machine. Annals of Statistics 29, 1189–1232.

Fritz, D., Rinck, D., Dillmann, R., Scheuring, M., 2006. Segmentation of the left and right cardiac ventricle using a combined bi-temporal statistical model, in: SPIE Medical Imaging, pp. 605–614.

Gassner, E., Ionasec, R.I., Georgescu, B., Vogt, S., Schoepf, U., Comaniciu, D., 2008. Performance of a dynamic aortic valve model for quantification of the opening area at cardiac mdct . comparison to manual planimetry, in: Radiological Society of North American (RSNA), Chicago, USA.

Grbić, S., Ionasec, R., Vitanovski, D., Voigt, I., Wang, Y., Georgescu, B., Navab, N., Comaniciu, D., 2010. Complete valvular heart apparatus model from 4D cardiac CT. Medical image computing and computer-assisted intervention : MICCAI ... International Conference on Medical Image Computing and Computer-Assisted Intervention 13, 218–26.

Halpern, E., 2008. Clinical Cardiac CT: Anatomy and Function. Thieme Medical Publishers, New York, NY , USA.

Hertz, T., 2006. Learning distance functions: algorithms and applications. Ph.D. thesis. The Hebrew University of Jerusalem.

Huang, J., Huang, X., Metaxas, D., Axel, L., 2007. Dynamic texture based heart localization and segmentation in 4-d cardiac images. Biomedical Imaging From Nano to Macro 2007 ISBI 2007 4th IEEE International Symposium on , 852–855.

Ionasec, R.I., et al., 2009. Robust motion estimation using trajectory spectrum learning: Application to aortic and mitral valve modeling from 4d tee, in: Proc. Int'l Conf. Computer Vision.

Ionasec, R.I., Georgescu, B., Comaniciu, D., Vogt, S., Schoepf, U., Gassner, E., 2008a. Patient specific 4d aortic root models derived from volumetric image data sets, in: Radiological Society of North American (RSNA), Chicago, USA.

Ionasec, R.I., Georgescu, B., Gassner, E., Vogt, S., Kutter, O., Scheuering, M., Navab, N., Comaniciu, D., 2008b. Dynamic model-driven quantification and visual evaluation of the aortic valve from 4d ct, in: MICCAI, pp. 686 – 694.

Ionasec, R.I., Voigt, I., Georgescu, B., Houle, H., Hornegger, J., Navab, N., Comaniciu, D., 2009a. Personalized Modeling and Assessment of the Aortic-Mitral Coupling from 4D TEE and CT, in: MICCAI, Heidelberg. pp. 767–775.

Ionasec, R.I., Voigt, I., Georgescu, B., Wang, Y., Houle, H., Vega-Higuera, F., Navab, N., , Comaniciu, D., 2010. Patient-specific modeling and quantification of the aortic and mitral valves from 4-D cardiac CT and TEE. IEEE transactions on medical imaging 29, 1636–51.

Ionasec, R.I., Wang, Y., Georgescu, B., Voigt, I., Navab, N., Comaniciu, D., 2009b. Robust motion estimation using trajectory spectrum learning: Application to aortic and mitral valve modeling from 4d tee, in: Proceedings of the Twelfth International Conference on Computer Vision (ICCV), IEEE, Kyoto, Japan.

Jablokow, A., 2009. National center for health statistics: National hospital discharge survey: Annual summaries with detailed diagnosis and procedure data. Data on Health Resources Utilization 13.

Kunzelman, K., Einstein, D., Cochran, R., 2007. Fluid-structure interaction models of the mitral valve: function in normal and pathological states. Philos. Trans. R. Soc. Lond., B, Biol. Sci. 362, 1393–1406.

Lansac, E., Lim, H., Shomura, Y., Lim, K., Rice, N., Goetz, W., Acar, C., Duran, C., 2002. A four-dimensional study of the aortic root dynamics. European journal of cardio-thoracic surgery : official journal of the European Association for Cardiothoracic Surgery 22, 497–503.

Lloyd-Jones, D., Adams, R., Carnethon, M., De Simone, G., Ferguson, T.B., Flegal, K., Ford, E., Furie, K., Go, A., Greenlund, K., Haase, N., Hailpern, S., Ho, M., Howard, V., Kissela, B., Kittner, S., Lackland, D., Lisabeth, L., Marelli, A., McDermott, M., Meigs, J., Mozaffarian, D., Nichol, G., O'Donnell, C., Roger, V., Rosamond, W., Sacco, R., Sorlie, P., Stafford, R., Steinberger, J., Thom, T., Wasserthiel-Smoller, S., Wong, N., Wylie-Rosett, J., Hong, Y., American Heart Association Statistics Committee and Stroke Statistics Subcommittee, 2009. Heart disease and stroke statistics–2009 update: a report from the american heart association statistics committee and stroke statistics subcommittee. Circulation 119, e21–181.

Lorenz, C., von Berg, J., 2006. A comprehensive shape model of the heart. Medical Image Analysis 10, 657–670.

Mutlak, D., Aronson, D., Lessick, J., Reisner, S., Dabbah, S., Agmon, Y., 2009. Functional tricuspid regurgitation in patients with pulmonary hypertension. CHEST , 115–121.

Osada, R., Funkhouser, T., Chazelle, B., Dobkin, D., 2002. Shape distributions. ACM Trans. Graph. 21, 807–832.

Park, J., Metaxas, D., Young, A., Axel, L., 1996. Deformable models with parameter functions for cardiac motion analysis from tagged mri data. IEEE Trans. Medical Imaging 15, 278–289.

Parr, J., Kirklin, J., Blackstone, E., 1977. The early risk of re-replacement of aortic valves. The Annals of Thoracic Surgery 23, 319–322.

Peskin, C.S., McQueen, D.M., 1996. Case Studies in Mathematical Modeling: Ecology, Physiology, and Cell Biology. Prentice-Hall, Englewood Cliffs, NJ, USA.

Piazza, N., de Jaegere, P., Schultz, C., Becker, A., Serruys, P., Anderson, R., 2008. Anatomy of the aortic valvar complex and its implications for transcatheter implantation of the aortic valve. Circulation. Cardiovascular interventions 1, 74–81.

Rueckert, D., Burger, P., 1997. Geometrically deformable templates for shape-based segmentation and tracking in cardiac mr images, in: EMMCVPR '97: Proceedings of the First International Workshop on Energy Minimization Methods in Computer Vision and Pattern Recognition, Springer-Verlag, London, UK. pp. 83–98.

Schievano, S., Coats, L., Migliavacca, F., Norman, W., Frigiola, A., Deanfield, J., Bonhoeffer, P., Taylor, A., 2007a. Variations in right ventricular outflow tract morphology following repair of congenital heart disease: Implications for percutaneous pulmonary valve implantation. Journal of Cardiovascular Magnetic Resonance 9, 687–95.

Schievano, S., Migliavacca, F., Coats, S., Khambadkone, L., Carminati, M., Wilson, N., Deanfield, J., Bonhoeffer, P., Taylor, A., 2007b. Percutaneous pulmonary valve implantation based on rapid prototyping of right ventricular outflow tract and pulmonary trunk from mr data. Radiology 242, 490–49.

Schievano, S., Migliavacca, F., Coats, S., Khambadkone, L., Carminati, M., Wilson, N., Deanfield, J., Bonhoeffer, P., Taylor, A., 2007c. Percutaneous pulmonary valve implantation based on rapid prototyping of right ventricular outflow tract and pulmonary trunk from mr data. Radiology 242, 490–49.

Schneider, R.J., Perrin, D.P., Vasilyev, N.V., Marx, G.R., Del Nido, P.J., Howe, R.D., 2010. Mitral annulus segmentation from 3d ultrasound using graph cuts. IEEE Transactions on Medical Imaging 29, 1676–1687.

Soncini, M., Votta, E., Zinicchino, S., Burrone, V., Mangini, A., Lemma, M., Antona, C., Redaelli, A., 2009. Aortic root performance after valve sparing procedure: A comparative finite element analysis. Medical Engineering and Physics 31, 234 – 243.

Staib, L.H., Duncan, J.S., 1996. Model-based deformable surface finding for medical images. IEEE Transactions on Medical Imaging 15, 720–731.

Tenenbaum, J.B., de Silva, V., Langford, J.C., 2000. A global geometric framework for nonlinear dimensionality reduction. Science 290, 2319 – 2323.

Timek, T., Green, G., Tibayan, F., Lai, F., Rodriguez, F., Liang, D., Daughters, G., Ingels, N., Miller, D., 2003. Aorto-mitral annular dynamics. Ann Thorac Surg 76, 1944–1950.

Tsymbal, A., Huber, M., Zhou, S.K., 2010. Discriminative distance functions and the patient neighborhood graph for clinical decision support. Springer. chapter Advances in Computational Biology. p. (to appear).

Tu, Z., 2005. Probabilistic boosting-tree: Learning discriminative methods for classification, recognition, and clustering, in: ICCV 2005, pp. 1589–1596.

Veronesi, F., Corsi, C., Sugeng, L., Mor-Avi, V., Caiani, E., Weinert, L., Lamberti, C., Lang, R., 2009a. A study of functional anatomy of aortic-mitral valve coupling using 3D matrix transesophageal echocardiography. Circ Cardiovasc Imaging 2, 24–31.

Veronesi, F., Corsi, C., Sugeng, L., Mor-Avi, V., Caiani, E., Weinert, L., Lamberti, C., R.M., L., 2009b. A study of functional anatomy of aortic-mitral valve coupling using 3D matrix transesophageal echocardiography. Circ Cardiovasc Imaging 2, 24–31.

Vitanovski, D., Ionasec, R.I., Georgescu, B., Huber, M., Taylor, A., Hornegger, J., Comaniciu, D., 2009. Personalized pulmonary trunk modeling for intervention planning and valve assessment estimated from ct data, in: International Conference on Medical Image Computing and Computer-Assisted Intervention (MICCAI), London, USA. pp. 17 – 25.

Vitanovski, D., Tsymbal, A., Ionasec, R., Georgescu, B., Huber, M., Hornegger, J., Comaniciu, D., 2010. Cross-modality assessment and planning for pulmonary trunk treatment using ct and mri imaging, in: International Conference on Medical Image Computing and Computer-Assisted Intervention (MICCAI), Beijing, China.

Votta, E., Caiani, E., Veronesi, F., Soncini, M., Montevecchi, F., Redaelli, A., 2008. Mitral valve finite-element modelling from ultrasound data: a pilot study for a new approach to understand mitral function and clinical scenarios. Philos Transact A Math Phys Eng Sci. 366, 3411–3434.

Waechter, I., et al., 2010. Patient specific models for planning and guidance of minimally invasive aortic valve implantation, in: MICCAI 2010. Springer Berlin / Heidelberg. volume 6361 of *Lecture Notes in Computer Science*, pp. 526–533.

Watanabe, N., Ogasawara, Y., Yamaura, Y., Kawamoto, T., Toyota, E., Akasaka, T., Yoshida, K., 2005. Quantitation of mitral valve tenting in ischemic mitral regurgitation by transthoracic real-time three-dimensional echocardiography. J Am Coll Cardiol 45, 763–769.

Webb, G.I., 2000. Multiboosting: A technique for combining boosting and wagging. Machine Learning 40, 159–196.

Yang, L., Georgescu, B., Zheng, Y., Meer, P., Comaniciu, D., 2008. 3d ultrasound tracking of the left ventricle using one-step forward prediction and data fusion of collaborative trackers, in: IEEE Conference on Computer Vision and Pattern Recognition.

Zheng, Y., Barbu, A., Georgescu, B., Scheuering, M., Comaniciu, D., 2008. Four-chamber heart modeling and automatic segmentation for 3d cardiac ct volumes using marginal space learning and steerable features. IEEE TMI 27, 1668–1681.

Zhou, S.K., Georgescu, B., Zhou, X.S., Comaniciu, D., 2005. Image based regression using boosting method, in: ICCV, pp. 541–548.

Zhuang, X., Rhode, K.S., Razavi, R.S., Hawkes, D.J., Ourselin, S., 2010a. A registration-based propagation framework for automatic whole heart segmentation of cardiac mri. IEEE Transactions on Medical Imaging 29, 1612–1625.

Zhuang, X., Yao, C., Ma, Y.L., Hawkes, D., Penney, G., Ourselin, S., 2010b. Registration-based propagation for whole heart segmentation from compounded 3D echocardiography. IEEE. p. 10931096.